Green Chemistry

PAPER

View Article Online
View Journal | View Issue

Cite this: *Green Chem.*, 2026, **28**, 3243

Piezocatalytic oxidation of lignin-derived phenol to *p*-benzoquinone: a sustainable route for green polymerization inhibitors

Xinlei Ma,[a] Bo Zhang, *[a] Xin Huang,[b] Qing Xu[c] and Roger Ruan [d]

Received 14th November 2025,
Accepted 26th January 2026

DOI: 10.1039/d5gc06083d

rsc.li/greenchem

Conventional processes for the conversion of lignin-derived phenol to *p*-benzoquinone (*p*-BQ) are associated with environmental concerns and efficiency issues, which necessitates the development of greener and more selective alternatives. This study reports a sulfur vacancy-engineered 2H-MoS_2 piezoelectric catalyst that enables efficient phenol conversion under mild aqueous/air conditions. The optimized catalyst exhibits outstanding performance, achieving a 92.57% phenol conversion and a 66.56% *p*-BQ yield within 6 hours. Integrated experimental and theoretical studies elucidate that sulfur vacancies play a pivotal dual role. Beyond enhancing the material's piezoelectric response and optimizing charge carrier dynamics, they function critically within the reaction mechanism by (1) acting as active sites that promote the adsorption of phenol and the subsequent desorption of *p*-BQ, and (2) selectively modulating the proportion of hydroxyl radicals (•OH) among the various reactive species. This work clarifies the central role of defect engineering in modulating active species and product selectivity, offering a new strategy for the green valorization of lignin derivatives.

Green foundation

1. Currently, the industrial production of *p*-BQ primarily relies on the aniline oxidation process using manganese dioxide, yet this method suffers from substantial generation of waste acid and organic solvents, coupled with low raw material utilization. In this work, we modulate the sulfur vacancies in MoS_2 to achieve the selective conversion of phenol, a sustainable and readily accessible lignin-derived feedstock, to *p*-BQ in an aqueous phase at room temperature.
2. Through sulfur vacancy engineering without chemical reagents, ultrasound-assisted reaction in aqueous phase achieved 92.57% phenol conversion and 66.56% *p*-BQ yield (71.9% selectivity) in 6 hours, approximately 1.5 and 4.15 times higher, respectively, *versus* the vacancy-free sample.
3. The ultrasonic treatment disrupts the material's crystal structure, however, potentially causing metal leaching. Thus, optimizing the sulfur vacancy concentration is essential to enhance catalytic stability without compromising the high *p*-BQ yield.

1. Introduction

Lignin, the most abundant natural source of aromatic polymers, serves as a key renewable feedstock for producing high-value chemicals.[1] Among its various depolymerization products, phenol stands out as a pivotal intermediate that remains underutilized.[2] Despite its wide use in synthesizing resins, plastics, and pharmaceuticals, lignin-derived phenol remains underutilized due to inefficient conversion pathways. It is imperative to develop advanced catalytic strategies to fully unlock the potential of lignin-derived phenol, in pursuit of strategic goals for sustainable biorefining and a circular bioeconomy. Selective oxidation of phenol into high-value specialty chemicals represents a promising route, however, conventional oxidation methods are often associated with high environmental risks, unsatisfactory selectivity, and significant energy consumption.[3]

p-Benzoquinone (*p*-BQ) is a crucial target product in the valorization of phenol, playing an indispensable role as a polymerization inhibitor in industrial polymer production.[4] The global market for such inhibitors is expanding rapidly, driven by the rising demand for stable monomers in plastics manufacturing. Beyond its function in polymerization stabilization, *p*-BQ serves as a versatile intermediate, which is widely applied in the synthesis of pharmaceuticals, agrochemicals, and fine chemicals.[5] However, the current industrial pro-

[a]*Key Laboratory of Energy Thermal Conversion and Control of Ministry of Education and School of Energy and Environment, Southeast University, Nanjing, Jiangsu 210096, China. E-mail: bozhang@seu.edu.cn*
[b]*CAS Key Laboratory of Urban Pollutant Conversion Department of Environmental Science and Engineering, University of Science & Technology of China, Hefei 230026, China*
[c]*College of Ocean Engineering and Energy, Guangdong Ocean University, Zhanjiang, Guangdong 524000, China*
[d]*Center for Biorefining and Department of Bioproducts and Biosystems Engineering, University of Minnesota, St. Paul, MN 55108, USA*

duction of *p*-BQ primarily relies on the aniline oxidation process using manganese dioxide. This method suffers from substantial generation of waste acid and organic solvents, coupled with low raw material utilization.[3] Although electrochemical and photocatalytic oxidation routes have been extensively explored as greener alternatives for the oxidation of phenol to *p*-BQ, they still face considerable shortcomings in terms of environmental friendliness, reaction efficiency, and product selectivity.[6,7] Therefore, there is an urgent need to develop innovative catalytic systems that operate under mild conditions with high selectivity.

Piezocatalysis, an emerging mechanochemical approach, offers a revolutionary solution by utilizing mechanical energy to drive chemical conversions. Unlike conventional thermal catalysis or photochemical methods, piezocatalysis relies on the piezoelectric effect to drive reactions under ambient conditions, enabling the generation of reactive oxygen species (ROS) without external oxidants.[8] When mechanical stress is applied to piezoelectric materials such as $BaTiO_3$, MoS_2, or ZnO, a polarized electric field forms within the material, facilitating molecular oxygen activation and selective oxidation of organic substrates.[9] In recent years, piezocatalysis has gained increasing attention in the field of organic synthesis. Koji Kubota *et al.* first demonstrated that $BaTiO_3$ piezocatalysts can promote the coupling of aryl and boron-based compounds *via* a single-electron-transfer pathway under ball-milling conditions.[10] Subsequently, Liu *et al.* developed hybrid piezocatalysts that achieved selective oxidation of aromatic alcohols to aldehydes. These advances highlight the potential of piezocatalysis in selective oxidation reactions. Nevertheless, piezocatalysis has not been extensively explored for selective phenol oxidation, necessitating the development of high-performance systems.[11]

Molybdenum disulfide (MoS_2), a two-dimensional transition metal sulfide with a hexagonal crystal structure, has demonstrated significant potential in piezocatalysis due to its high carrier mobility, excellent mechanical flexibility, and tunable electronic properties.[12] However, pristine MoS_2 suffers from rapid electron–hole recombination and limited capabilities for adsorbing and activating reactants.[13] Among various strategies for performance enhancement, surface defect engineering, such as the introduction of sulfur vacancies, has attracted considerable attention for its ability to effectively modulate the electronic structure of materials.[14] Yang *et al.* discovered that precisely engineered sulfur vacancies synergistically enhanced the piezoelectric performance of $ZnIn_2S_4$ by concurrently optimizing its band structure and breaking its crystal symmetry, thereby inducing the simultaneous generation of multiple reactive oxygen species ($^{\bullet}O_2^-$, $^1O_2$, H_2O_2, and $^{\bullet}OH$) under ultrasonic irradiation.[15] Zhu *et al.* systematically revealed the regulatory mechanism of vacancy concentration differences on material crystallinity and catalytic rates, pointing out that atomic mismatch at crystal-amorphous interfaces with higher vacancy concentrations can introduce more active sites and significantly promote charge transport.[13]

Based on the above, MoS_2 materials with tunable sulfur vacancy concentrations were synthesized *via* a one-step hydrothermal method for the selective piezocatalytic oxidation of phenol to *p*-BQ. EPR characterization confirmed the successful construction of MoS_2 catalysts with distinct sulfur vacancy densities. Beyond fundamental structural characterization, PFM was further employed to analyze the intrinsic relationship between sulfur vacancy concentrations and the piezoelectric properties of the materials. The critical role of sulfur vacancies in promoting charge carrier separation and migration was investigated using multiple characterization techniques. Through optimization of the reaction conditions, the catalytic performance was effectively enhanced. Radical quenching experiments and EPR results confirmed that the piezocatalytic pathway was dominated by hydroxyl radicals ($^{\bullet}OH$) and that the possible route of $^{\bullet}OH$ generation was investigated. Finally, integrated with density functional theory (DFT) calculations, the dual functional mechanism of sulfur vacancies in this piezocatalytic system was further elucidated. This study provides valuable insights and a practical framework for lignin valorization and the green synthesis of aromatic compounds based on defect engineering.

2. Experimental section

2.1. Materials and reagents

This section is presented in the SI.

2.2. Synthesis of catalysts

Both pristine MoS_2 and S-vacancy-rich MoS_2 were synthesized *via* a facile one-step hydrothermal method, with the sulfur vacancy concentration controlled by modulating the initial thiourea amount. Catalysts with varying sulfur vacancy concentrations were synthesized and denoted as MS-2, MS-3, and MS-4. For comparison, a control sample (MS-1) with negligible sulfur vacancies was prepared using an identical procedure but with a different thiourea concentration. Specifically, while the amount of ammonium molybdate tetrahydrate was fixed at 1 mmol, the initial quantities of thiourea for MS-2, MS-3, and MS-4 were 14 mmol, 28 mmol, and 42 mmol, respectively. In a typical synthesis, the reactants were dissolved in 30 mL of deionized water and vigorously stirred for 3 hours to form a homogeneous solution. This solution was then transferred into a 100 mL Teflon-lined stainless-steel autoclave and maintained at 200 °C for 18 hours. After natural cooling to room temperature, the resulting solid product was collected and repeatedly washed with ethanol and deionized water, followed by centrifugation at 5000 rpm for 8 minutes. The product was then dried overnight in a vacuum oven at 60 °C. The final catalyst was obtained by grinding the dried powder and sieving it through a 0.45 mm mesh. The synthesis method for the MIX catalyst is also provided in the SI.

2.3. Experimental procedure

The piezocatalytic reaction was driven by mechanical vibration provided by an ultrasonic cleaner (DS-5510DTH) operating at a fixed power output and a frequency of 40 kHz. In a typical pro-

cedure, 30 mL of a 0.2 mM phenol solution was transferred into a 50 mL beaker, followed by the addition of a specific mass of the catalyst. To further investigate the catalyst's performance under different substrate concentrations, experiments were also extended to initial phenol concentrations of 0.5 mM and 1 mM for comparison. The beaker was securely positioned inside the ultrasonic bath using an iron stand and a tube holder to ensure stability. To eliminate the influence of heat generated during ultrasonication, the temperature was maintained at 25 °C using an external circulating cooling water system. After the reaction, the solution was collected and filtered through a 0.22 μm membrane to remove the solid catalyst. The filtrate was then transferred into a vial for HPLC analysis. The concentrations of phenol and *p*-BQ were determined by HPLC based on their respective peak areas and calibration curves. To reuse the catalyst, it was recovered from the mixture by suction filtration, washed repeatedly with ethanol and deionized water, and dried in a vacuum oven at 60 °C. Additional experimental information is available in the SI.

The phenol conversion and *p*-BQ yield were calculated using the following equations:

$$\text{Phenol conversion}\,(\%) = \frac{n(\text{phenol consumed})}{n(\text{phenol initial})} \times 100\% \quad (1)$$

$$p\text{-BQ yield}\,(\%) = \frac{n(p\text{-BQ formed})}{n(\text{phenol initial})} \times 100\% \quad (2)$$

$$p\text{-BQ selectivity}\,(\%) = \frac{n(p\text{-BQ formed})}{n(\text{phenol consumed})} \times 100\% \quad (3)$$

2.4. Characterizations

This section is presented in the SI.

2.5. Electrochemical measurements

Electrochemical measurements, including transient piezoelectric response (TPR), electrochemical impedance spectroscopy (EIS), and Mott–Schottky (MS) analysis, were performed using an electrochemical analyzer (DH7000C, DongHua Analytica, China) in a three-electrode. The system employed the sample as the working electrode, an Ag/AgCl reference electrode, and a Pt plate counter electrode. All measurements were conducted in a 1 M KOH aqueous electrolyte. All ITO glass substrates (1 cm × 2 cm) were sequentially cleaned *via* ultrasonication in deionized water and ethanol for 30 minutes. The working electrode was prepared by dispersing 10 mg of the synthesized sample in a mixed solution containing 400 μL deionized water, 100 μL ethanol, and 50 μL Nafion solution, followed by 2 hours of ultrasonication to form a homogeneous ink. Subsequently, 100 μL of the resulting ink was drop-cast onto the ITO substrate and allowed to dry naturally in air for 24 hours. The exposed geometric area of the working electrode immersed in the electrolyte was controlled at 1 cm^2.

2.6. DFT calculations

This section is presented in the SI.

3. Results and discussion

3.1. Morphology and physical properties

The MoS_2 samples were prepared by a one-step hydrothermal process, as illustrated schematically in Fig. 1a. By modulating the thiourea concentration, we obtained a series of MoS_2 samples with different sulfur vacancy concentrations, which were labeled MS-2 (low vacancy), MS-3 (moderate vacancy), and MS-4 (high vacancy). MS-1, prepared without deliberate vacancy introduction, served as the reference catalyst. As shown in Fig. 1b–e, all samples exhibited a petal-like morphology assembled from interconnected thin nanosheets. This observation indicated that the introduction of sulfur vacancies did not alter the fundamental microstructure.[16] TEM images of MS-3 (Fig. 1f and g) further confirmed its well-defined nanoflower architecture. TEM images of the edge regions (Fig. 1h and i) revealed stacked monolayer or few-layer nanosheets. The high-resolution TEM image in Fig. 1j showed lattice fringes with an interplanar spacing of approximately 0.615 nm, corresponding to the (002) plane of MoS_2.[17] Local lattice distortions were visible in the circled regions. The selected-area electron diffraction (SAED) pattern in Fig. 1k exhibited clear diffraction rings, confirming that the material retained good crystallinity after the introduction of sulfur vacancies. Furthermore, elemental mapping results (Fig. 1l) demonstrated a homogeneous distribution of Mo and S, affirming the uniform composition of the synthesized MoS_2.

EPR analysis (Fig. 2a) confirms the presence of sulfur vacancies, with a characteristic signal at $g \approx 2.003$.[18] The signal intensity showed a clear enhancement from MS-1 to MS-4, qualitatively demonstrating the successful synthesis of MoS_2 with a graded concentration of sulfur vacancies. The crystalline phase of the four catalysts was investigated using X-ray diffraction (XRD), as presented in Fig. 2b. All samples exhibited distinct diffraction peaks at 2θ values of 14.4°, 32.7°, and 58.3°, which can be indexed to the (002), (100), and (110) crystal planes of MoS_2 (PDF#37-1492).[19] The dominant peak at 2θ = 14.4°, corresponding to the (002) plane, indicates a preferentially oriented stacking of the nanoflower architecture.[20] Raman spectroscopy was employed to investigate the structural features of the samples (Fig. S1). All samples exhibited two characteristic Raman peaks in the ranges of 380–385 cm^{-1} and 402–405 cm^{-1}, which are assigned to the in-plane (E^1_{2g}) and out-of-plane (A_{1g}) vibrational modes of MoS_2, respectively.[21,22] A systematic decrease in the peak spacing (Δ) between the E^1_{2g} and A_{1g} modes was observed with increasing sulfur vacancy concentration. This trend, accompanied by a red-shift of the E^1_{2g} peak, collectively signified a reduction in lattice symmetry.[23]

X-ray photoelectron spectroscopy (XPS) was employed to further investigate the influence of sulfur vacancies on the electronic structure of the materials. As shown in Fig. 2c and d, the characteristic peaks of both Mo and S elements correspond to the structural features of the 2H phase in MoS_2.[24] The Mo 3d XPS spectrum of MS-1 can be deconvoluted into three characteristic peaks with binding energies located at 229.01 eV, 232.13 eV, and 226.67 eV, corresponding to Mo $3d_{5/2}$, Mo $3d_{3/2}$, and the

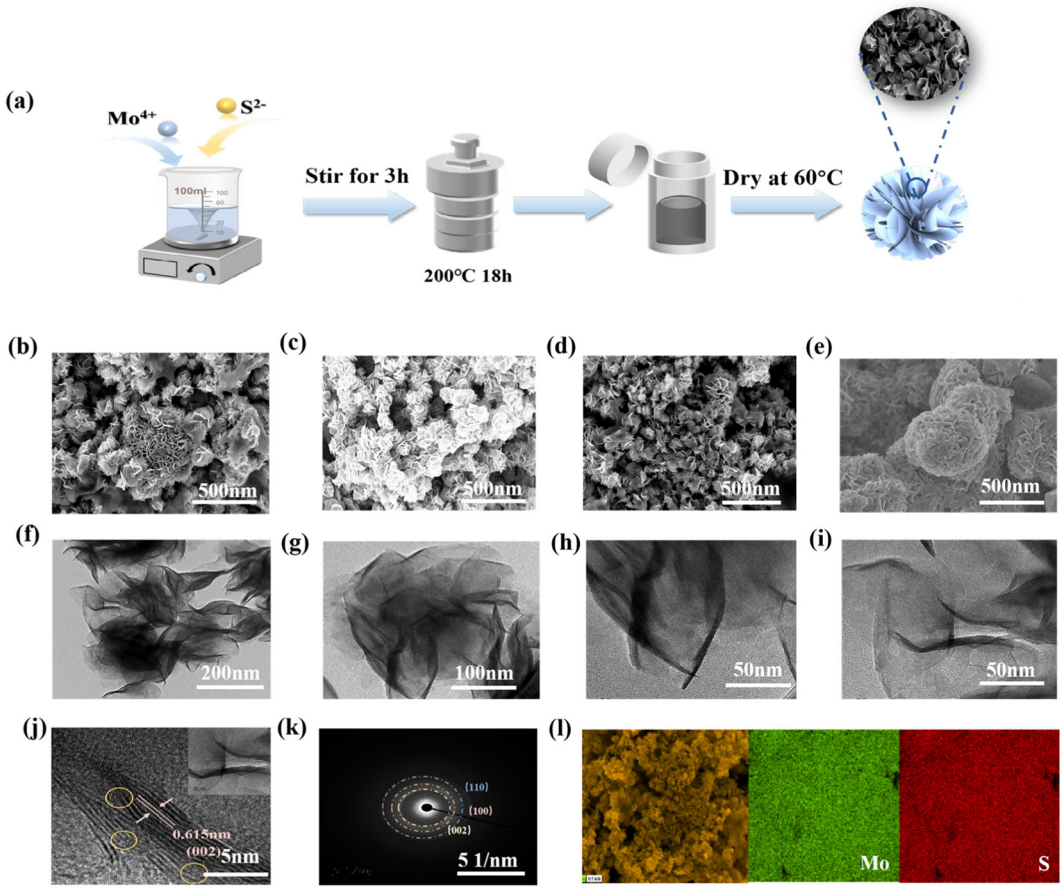

Fig. 1 (a) Hydrothermal route for MoS_2 synthesis; SEM image of (b) MS-1, (c) MS-2, (d) MS-3 and (e) MS-4; TEM images (f) and (g) of MS-3; TEM image (h) and (i) of the edge region of MS-3; (j) HRTEM image of MS-3; (k) SAED pattern of MS-3; (l) corresponding element (Mo and S) mapping of MS-3.

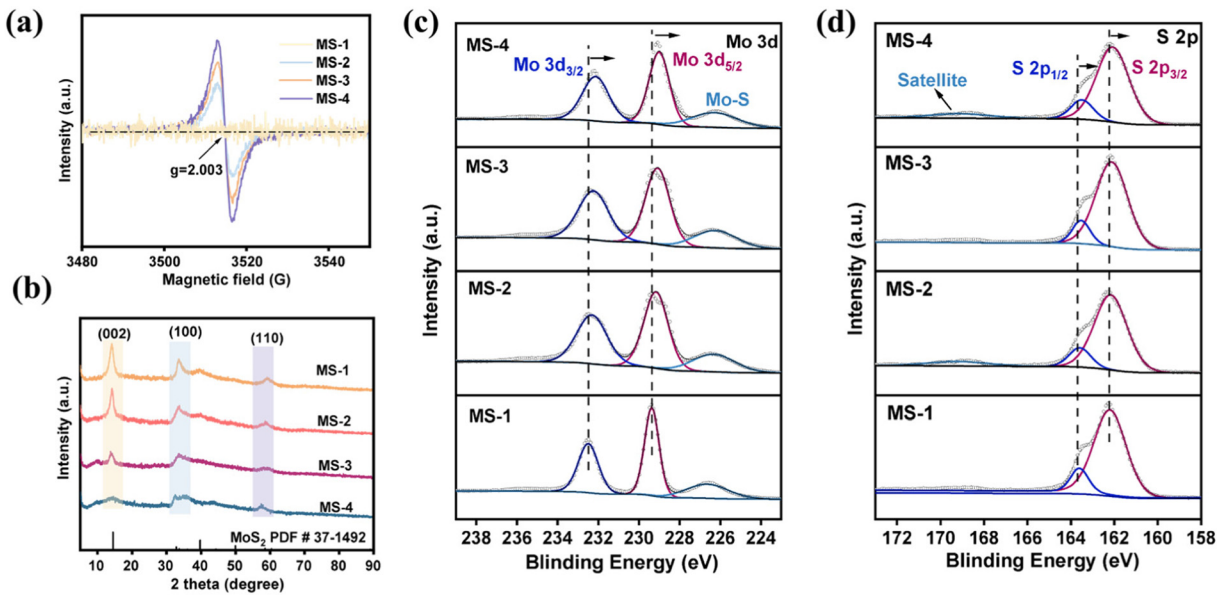

Fig. 2 (a) EPR spectra of the MS-1, MS-2, MS-3 and MS-4 samples; (b) XRD patterns of the four samples; high-resolution XPS spectra of (c) Mo 3d and (d) S 2p for the MS-3 sample.

Mo–S bond, respectively. Similarly, the S 2p spectrum is fitted with two characteristic peaks at binding energies of 162.20 eV and 163.60 eV, assigned to S $2p_3/_2$ and S $2p_1/_2$, respectively.[25] As the sulfur vacancy concentration increases, the enhanced electron density around Mo^{4+} results in a negative shift in the binding energy of the Mo 3d XPS peaks. Similarly, the binding energy of S^{2-} bonded to Mo^{4+} also exhibits a negative shift.[15,26] Furthermore, the chemical environment around Mo atoms is more significantly affected by sulfur vacancies, leading to a more pronounced shift in its binding energy (approximately 0.36 eV) compared to that of *S* (approximately 0.11 eV). Such an asymmetric shift behavior has been reported in the literature.[15,27] The observed binding energy shifts directly confirmed that the introduction of sulfur vacancies effectively modulated the electronic structure of MoS_2, providing a structural basis for understanding the enhanced catalytic performance.

The piezocatalytic process comprises two consecutive stages. It initiates with the generation of polarized charges under mechanical stress, governed by the material's intrinsic piezoelectricity. Subsequently, these separated charges migrate to the catalyst surface to drive redox reactions with adsorbed molecules, and thus the overall efficiency is governed by charge carrier separation and migration.[8] Previous studies have indicated that the introduction of sulfur vacancies can significantly modulate the piezoelectric properties by enhancing the asymmetry of the crystal structure.[28] Accordingly, we systematically evaluated the piezoelectric behavior of all samples using piezoelectric force microscopy (PFM).

The piezoelectric coefficients (D_{33}) were quantitatively analyzed from the D_{33} curves (Fig. 3a–d), yielding values of 11.68, 15.66, 86.48, and 35.72 pm V^{-1} for MS-1 to MS-4, respectively. Notably, the D_{33} value of MS-3 was approximately 7.4 times higher than that of MS-1, demonstrating that moderate sulfur vacancy engineering effectively enhances the piezoelectric performance of MoS_2. Under an AC bias of ±10 V, all samples exhibited characteristic butterfly-shaped amplitude curves and 180° phase hysteresis loops (Fig. 3e–h), confirming their pronounced piezoelectric responses. While MS-1 showed the smallest amplitude and displacement, samples with sulfur vacancies (MS-2 to MS-4) displayed significantly stronger displacement responses. In particular, MS-3 achieved a maximum amplitude of 11 nm, 13.75 times greater than that of MS-1 (0.8 nm). This significantly enhanced piezoelectric performance manifests as a stronger piezoelectric potential and a greater quantity of polarized charges, thereby boosting the catalytic efficiency.[29] These results reveal a limited piezoelectric enhancement from a low sulfur vacancy concentration, with MS-2 exhibiting only a modest 1.34-fold D_{33} increase over MS-1. Excessive sulfur vacancies are detrimental to piezoelectric performance due to a decline in crystallinity, which is consistent with XRD results and the literature.[13,30]

3.2. Charge separation and band structures

The enhancement of piezocatalytic performance is often limited by issues such as slow separation and migration of polarized charges and their facile recombination.[31] To explore the influence of sulfur vacancies on carrier dynamics, the charge separation efficiency of the four catalysts was first evaluated using photoluminescence (PL) spectroscopy. PL intensity is positively correlated with the recombination rate of photogenerated carriers, higher intensity indicates a greater tendency for electron–hole pair recombination.[32] As shown in Fig. 4a, the photoluminescence (PL) intensity of the materials with introduced sulfur vacancies is significantly lower than that of MS-1. MS-3, with a moderate vacancy concentration, showed the lowest intensity (approximately a quarter that of MS-1), indicating optimal charge separation. In contrast, MS-4, despite its possession of the highest sulfur vacancy concentration, exhibited inferior charge separation efficiency. Electrochemical impedance spectroscopy (EIS) was further employed to study charge transfer behavior (Fig. 4b). The charge transfer resistance (R_{ct}), corresponding to the arc radius of the Nyquist plot, is inversely proportional to the interfacial charge transfer rate.[14] The electrical resistance decreased significantly from MS-1 to MS-3 with increasing sulfur vacancy concentration. The enhanced conductivity of materials is primarily attributed to a synergistic mechanism: the reduction in crystallinity intensifies structural disorder, which broadens the charge transport pathways,[13] meanwhile, the sulfur vacancies act as electron donors, effectively increasing the density of free charge carriers.[33] However, the charge transfer efficiency declines in MS-4 with its higher sulfur vacancy concentration. This trend is consistent with the PL results, as excessive sulfur vacancies can act as recombination centers, thereby impairing charge separation and transport.[26] The trend observed in the EIS data is consistent with the transient piezoelectric current response (*i*–*t* curves) of the four materials. As shown in Fig. 4c, under pulsed mechanical stimulation simulated by periodic ultrasound on/off cycles, MS-3 exhibited the strongest piezoelectric current response, followed by MS-2, while MS-1 showed the weakest response. Collectively, these analyses demonstrated that an appropriate concentration of sulfur vacancies effectively facilitates the separation and migration of piezoelectric charges in MoS_2.[34,35] The piezoelectric current response of MS-3 was further evaluated under ultrasonic power levels ranging from 60 W to 300 W (Fig. 4d). The current amplitude increased steadily with rising power input and maintained good stability, confirming the excellent robustness of the piezoelectric performance.

The role of sulfur vacancies in modulating the band structure was first investigated by characterizing the optical properties of the MS-1 to MS-4 samples using UV-Vis absorption spectroscopy (Fig. 4e). MS-1 showed two characteristic excitonic absorption peaks at 605 nm and 666 nm, resulting from excitonic transitions permitted by its ordered crystal structure.[36] With the introduction of sulfur vacancies, the intensity of these excitonic peaks decreased markedly (see the light-yellow highlighted region), indicating that vacancy-induced defect states disrupted the periodic lattice potential and localize charge carriers, thereby suppressing exciton formation and altering the optical absorption behavior.[23] The bandgap energies (E_g) of the four materials were determined from the

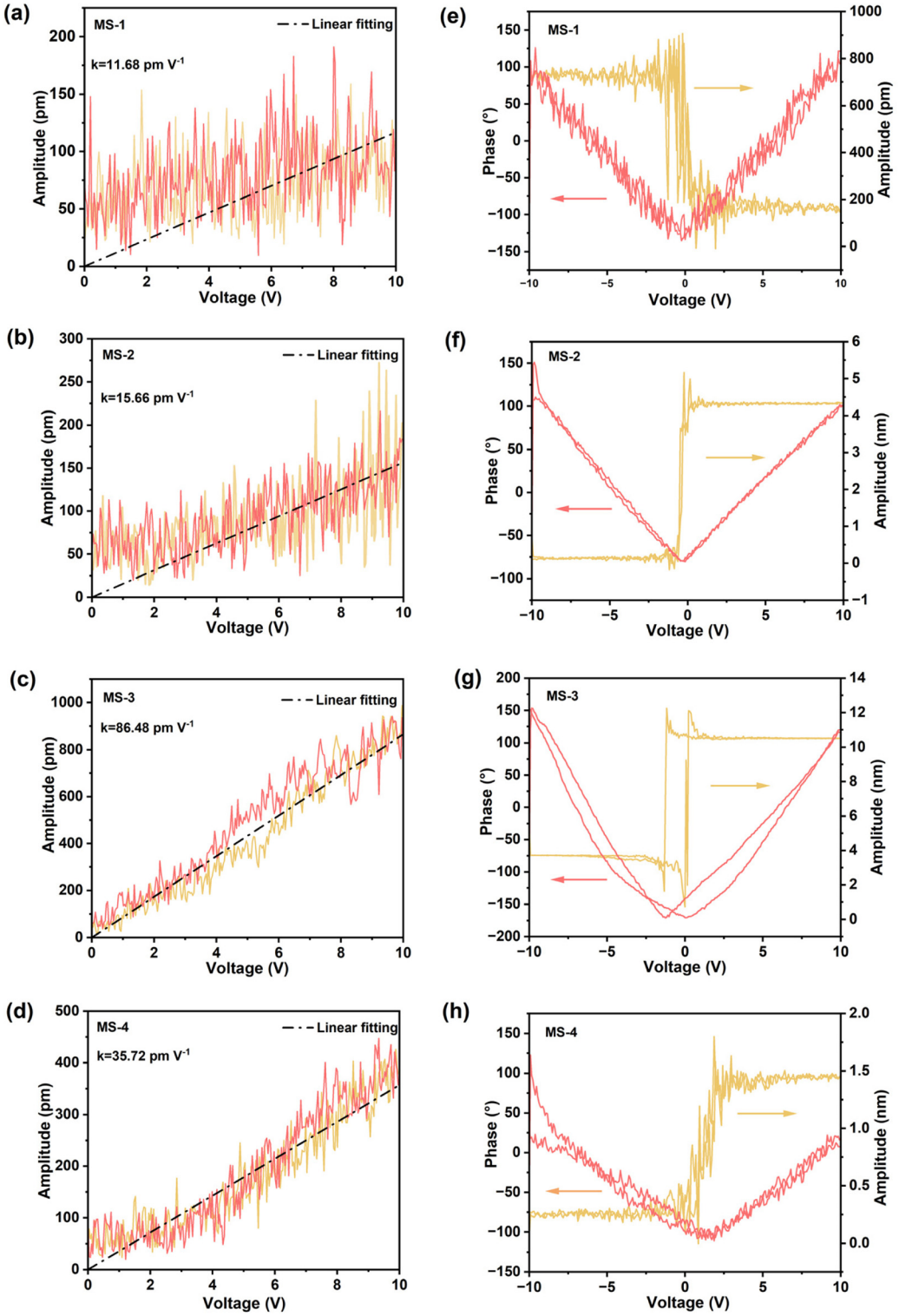

Fig. 3 PFM analysis: piezoelectric strain coefficient D_{33} curves: (a) MS-1, (b) MS-2, (c) MS-3 and (d) MS-4; butterfly-shaped amplitude curve and hysteresis loop of (e) MS-1, (f) MS-2, (g) MS-3 and (h) MS-4.

UV-Vis data using the Tauc plot method (eqn (S4), SI), treating MoS_2 as a direct bandgap semiconductor (n = 1).[37] As shown in Fig. 4f, the obtained E_g values for MS-1, MS-2, MS-3, and MS-4 are 1.84 eV, 1.26 eV, 1.13 eV, and 1.03 eV, respectively. The marked reduction in bandgap with increasing sulfur vacancy concentration is attributed to defect levels formed between the valence and conduction bands, leading to band narrowing.[35] Mott–Schottky measurements were conducted at

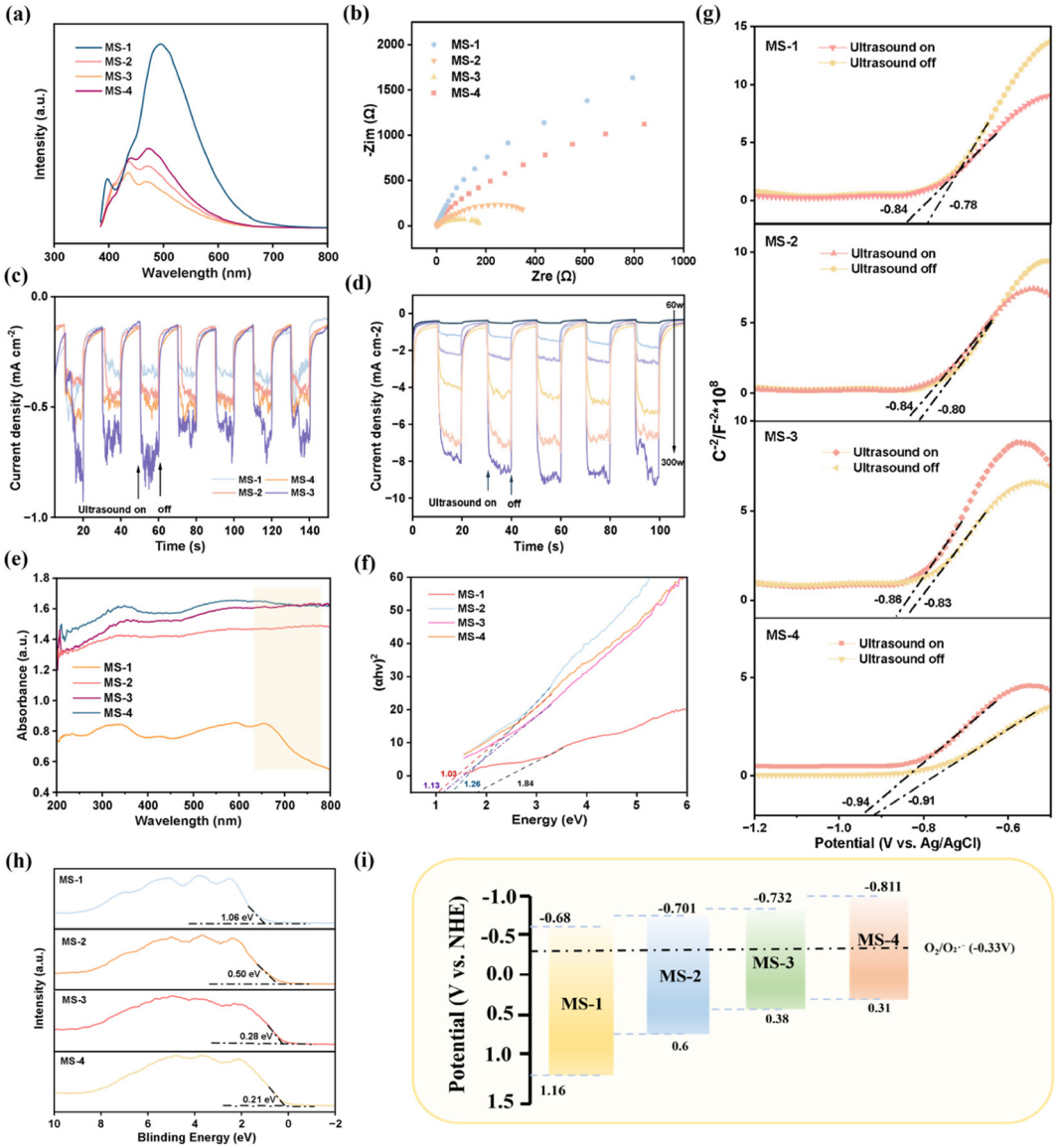

Fig. 4 (a) Steady-state photoluminescence (PL) spectra of MS-1, MS-2, MS-3 and MS-4; (b) EIS spectra of the four samples; (c) piezo-response currents of the four samples; (d) piezo-response currents of MS-3 under different ultrasonic power (60W-300 W); (e) UV-vis diffuse reflectance spectra of the four samples; (f) Tauc' s bandgap plots of four samples (n = 1); (g) ultrasound (90 W, 40 kHz) on/offresponse and 1 kHz Mott–Schottky curves of MS-1 to MS-4; (h) VB-XPS of all the samples; (i) band structure diagrams of the four samples.

1 kHz to characterize the four catalysts (Fig. 4g). All samples exhibited positive slopes in their M–S plots, confirming n-type semiconductor behavior. The flat-band potentials (E_{fb}) relative to Ag/AgCl were determined from the curve intercepts as −0.78 V, −0.80 V, −0.83 V, and −0.91 V for MS-1 to MS-4, respectively. After conversion to the standard hydrogen electrode (NHE) scale using eqn (S5) (SI), these potentials were determined to be −0.58 V, −0.601 V, −0.632 V, and −0.711 V, the conduction band potential (E_{cb}) is generally about 0.1 V more negative than E_{fb}. Accordingly, the estimated E_{cb} values for MS-1 to MS-4 were −0.68 V, −0.701 V, −0.732 V, and −0.811 V (*vs.* NHE). A continuous negative shift in E_{fb} was observed with increasing sulfur vacancy concentration, indicating a systematic upward shift of the Fermi level. This trend promotes optimized band bending and enhances the interfacial built-in electric field in the n-type semiconductors.[38] A gradual decrease in the valence band maximum with increasing sulfur vacancy content was observed in the Valence band X-ray photoelectron spectroscopy (VB-XPS, Fig. 4h), consistent with the trend from the Mott–Schottky measurements.[23] The E_{VB} values relative to NHE were calculated as 1.16 V, 0.50 V, 0.28 V, and 0.21 V for MS-1 to MS-4, respectively, using eqn (S6) (SI). Based on these results, a schematic band structure diagram was constructed, as shown in Fig. 4i.

Under ultrasonic actuation, Mott–Schottky measurements revealed a consistent negative shift in the flat-band potential across all catalysts, demonstrating piezoelectric field-mediated band structure regulation (Fig. 4g). This shift indicates Fermi

level realignment, which enhances the built-in electric field to drive charge separation and suppress recombination.[39] Collectively, these results verify that sulfur vacancy engineering enhances both the static interfacial field and the dynamic polarization field from the piezoelectric effect.[40]

3.3. Piezocatalytic conversion of phenol to *p*-benzoquinone

To investigate the performance of the piezoelectric catalytic system in the selective oxidation of phenol to *p*-BQ, an ultrasonic reactor was employed as the mechanical energy source, and the reaction temperature was maintained at 25 °C using a circulating water bath to exclude thermal effects. The standard curves for phenol and *p*-BQ are shown in Fig. S2. The catalytic performances of the four catalysts with different sulfur vacancy concentrations were evaluated. As shown in Fig. 5a, MS-3 exhibited the optimal catalytic activity. Compared to MS-1, it achieved a 1.4-fold increase in phenol conversion and a remarkable 4.35-fold enhancement in *p*-BQ yield. MS-2 showed lower activity than MS-3 due to its weaker piezoelectric performance. The performance decline of MS-4 can be attribu-

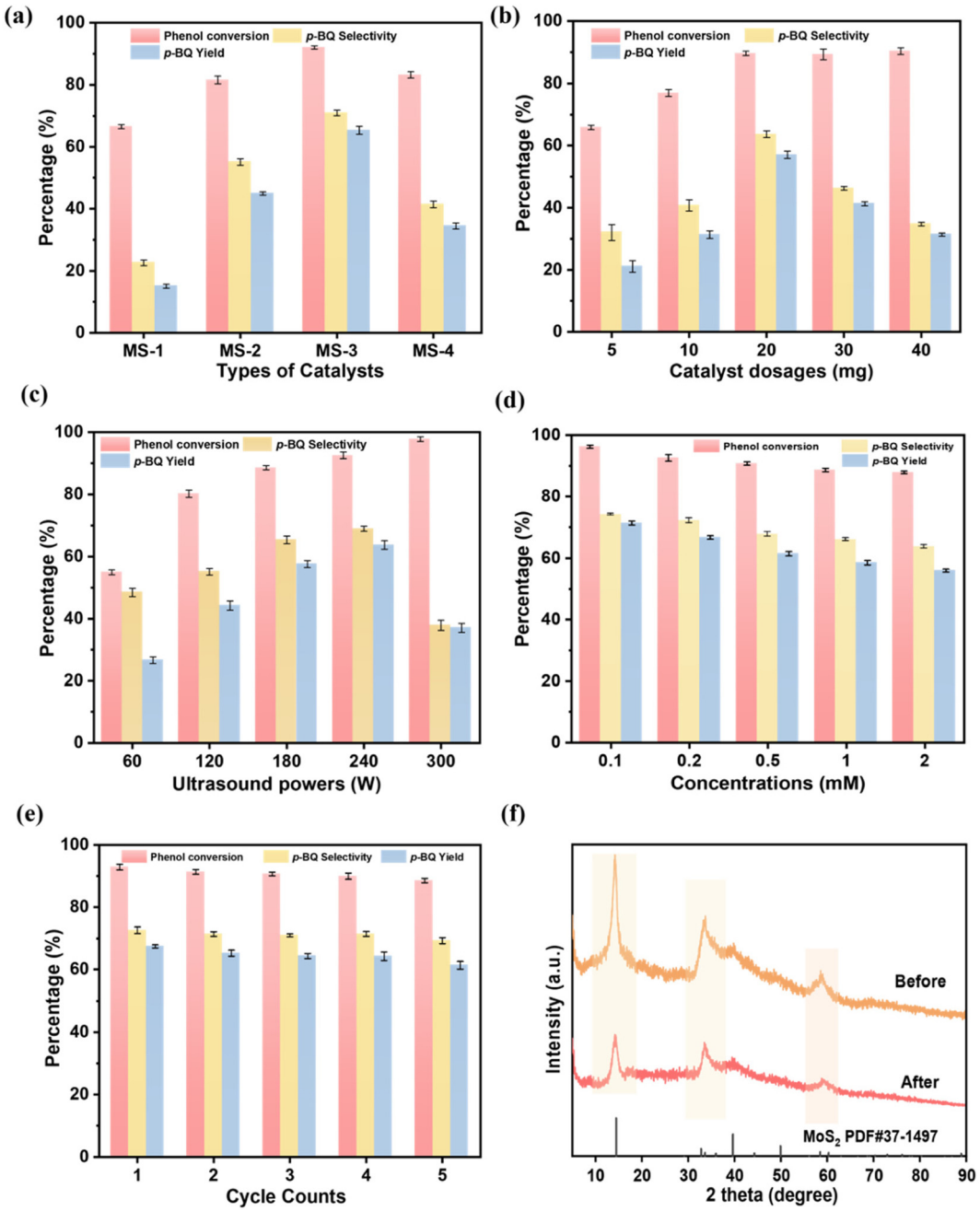

Fig. 5 Effects of various factors on the piezocatalytic conversion of phenol to *p*-BQ: (a) types of catalysts (20 mg, 240 W); (b) catalyst dosages (180 W); (c) ultrasound powers (20 mg); (d) phenol concentrations (20 mg, 240 W); (e) cycling tests; (f) XRD patterns of MS-3 before and after the reaction.

ted to the fact that the excessive vacancies may act as recombination centers for piezoelectric charges, thereby suppressing the effective separation of charge carriers.[41] Furthermore, the effects of key parameters, including catalyst dosages, ultrasonic powers, and phenol concentrations, were systematically evaluated. As shown in Fig. 5b and c, although excessive catalyst dosage and elevated ultrasonic power further increased phenol conversion, they resulted in a significant decrease in both the yield and selectivity of *p*-BQ. This is likely due to over-oxidation under such conditions, leading to further oxidation of phenol. The corresponding piezoelectric current response at 300 W ultrasonic power is shown in Fig. 4d. Notably, the MS-3 catalyst demonstrated broad adaptability to substrate concentration, maintaining stable catalytic performance over a phenol concentration range of 0.1–2 mM (Fig. 5d). Ultimately, under optimized conditions, this system achieved 92.57% phenol conversion in 6 h, with a *p*-BQ yield of 66.56% and 71.9% selectivity. As summarized in Table S1 (SI), the piezocatalytic performance in this work is comparable to that of existing catalytic systems.

To evaluate the cycling stability of the catalyst, recycling and reuse experiments were conducted on the MS-3 sample. As shown in Fig. 5e, after five consecutive cycles, the phenol conversion decreased by only 3.32%, and the *p*-BQ yield declined by 5.112%, indicating good operational stability of the catalyst. To assess the structural stability, the used MS-3 catalyst from the cycling experiments was characterized by SEM, XRD, and XPS. SEM and TEM images of the catalyst before and after cycling (Fig. S3) reveal that the cycled sample largely retains its overall architecture, which is predominantly composed of clusters of wrinkled nanosheets. This observation indicates that the fundamental framework of the material remains preserved. However, compared to the pristine catalyst, the cycled sample exhibits partially dispersed edges of the nanosheet clusters, along with a structural transition from tightly stacked layers to a relatively looser and slightly expanded morphology in localized regions. In the XRD pattern (Fig. 5f), a discernible attenuation in diffraction peak intensity was observed, yet the primary crystal structure was essentially preserved, indicative of its robust structural stability. These findings were further corroborated by the XPS analysis (Fig. S4). To assess the practical applicability of the catalytic system under realistic conditions, the piezocatalytic performance of MS-3 was evaluated in the presence of typical lignin-derived phenolic impurities. Guaiacol, syringol, and an equimolar mixture of both were separately introduced into a 0.2 mM phenol solution, each at a concentration corresponding to 5% of the phenol concentration. As shown in Fig. S5, despite the presence of these competing phenolic species, all impurity-containing systems maintained high catalytic performance, with phenol conversions above 87% and *p*-BQ yields above 60%, compared to the control. Selectivity toward *p*-BQ remained consistently above 68% across all tests. These findings indicate that both activity and selectivity are well preserved under impurity-containing conditions, highlighting the system's strong tolerance toward typical lignin-derived interferents. Thus, this catalytic system demonstrates promising potential for the valorization of real, multicomponent lignin-derived phenolic feedstocks.

Among the primary phase structures of MoS_2, the 2H phase is a thermodynamically stable, non-centrosymmetric semiconductor and serves as the main source of piezoelectric activity, although its electrical conductivity is relatively limited.[42,43] In contrast, the 1T phase is a metastable metallic phase with a centrosymmetric structure that exhibits no piezoelectric response but possesses excellent conductivity and metal-like characteristics.[44,45] The comparison of MIX and MS-3 in conductivity, piezoelectric response, and catalytic activity elucidates the role of MoS_2 phase structure in the piezocatalytic conversion of phenol to *p*-BQ.

The XRD, Raman spectroscopy, and XPS characterizations of MIX (Fig. S6a–d) confirm the successful incorporation of the 1T-phase MoS_2, with quantitative XPS analysis indicating a 1T-phase content as high as ~65%. Although the incorporation of the 1T phase significantly reduces the charge transfer resistance of the material (Fig. S6g), its centrosymmetric structure also substantially weakens the intrinsic piezoelectric response, yielding a D_{33} coefficient of only 10.29 pm V^{-1} (Fig. S6e and f). In the piezocatalytic conversion of phenol, MIX exhibits much lower catalytic activity than the MS-series catalysts (Fig. S6h). The inferior catalytic performance of MIX primarily originates from its weak piezoelectric response: although the 1T phase facilitates charge migration, its inherently low piezoelectric effect leads to insufficient polarization charge generation under external stress, limiting effective carrier separation and migration, and ultimately reducing piezocatalytic activity.

Furthermore, Fig. S7 displays the optimized structure of 1T-MoS_2 containing a sulfur vacancy (Sv-1T-MoS_2), along with the calculated adsorption energies of phenol and O_2 on its surface. These results are compared with those of pristine 2H-MoS_2 and sulfur-vacancy-containing 2H-MoS_2 (Sv-2H-MoS_2) in Table S2. Relative to pristine 2H-MoS_2, introducing sulfur vacancies markedly enhances the material's adsorption capacity for both O_2 and phenol, confirming the role of sulfur vacancies as key active sites for adsorption. Moreover, the adsorption energies of oxygen and phenol on Sv-2H-MoS_2 are −2.323 eV and −0.615 eV, respectively, while those on Sv-1T-MoS_2 are −1.784 eV and −0.464 eV, respectively. These results indicate that the Sv-2H-MoS_2 exhibits stronger adsorption for both O_2 and phenol. Thus, both experimental and theoretical analyses confirm that under similar sulfur vacancy concentrations, the 1T-phase MoS_2 shows inferior piezocatalytic phenol conversion performance and lower selectivity toward *p*-BQ due to its weak piezoelectric response. This further demonstrates that the outstanding piezocatalytic conversion of phenol observed in the MS-series catalysts originates from the introduction of sulfur vacancies rather than from phase transformation.

3.4. Mechanistic insights into piezocatalytic process

Given the frequent detection of active radicals in piezoelectric catalysis and its mechanistic resemblance to photocatalysis,[46] 1,3-diphenylisobenzofuran (DPBF) was employed as a mole-

cular probe to verify the presence of reactive oxygen species (ROS) by monitoring its absorbance decay. ROS can oxidize the yellow DPBF into colorless 1,2-dibenzoylbenzene (DBB).[15] As shown in Fig. 6a, under ultrasonic excitation, the absorbance of DPBF in the presence of MS-3 decreased markedly over time, indicating significant ROS involvement. A comparative study of the four catalysts (Fig. 6b) revealed that MS-3 induced the most rapid DPBF decay under identical conditions, highlighting its superior ROS generation capability.

To identify the specific reactive species, quenching experiments were conducted with MS-3 using $AgNO_3$, EDTA-2Na, superoxide dismutase (SOD), isopropanol (IPA), and L-histidine (L-His) to scavenge e^-, h^+, $^{\bullet}O_2^-$, $^{\bullet}OH$, and $^1O_2$, respectively. As depicted in Fig. 6c, the addition of IPA ($^{\bullet}OH$ quencher) caused the most pronounced suppression, phenol conversion decreased by 66.49% compared to the control, and *p*-BQ formation was nearly completely inhibited. Furthermore, scavenging superoxide radicals ($^{\bullet}O_2^-$), electrons (e^-), or holes (h^+) all suppressed the catalytic process. The overall inhibitory efficacy of the quenchers followed the order of $^{\bullet}OH > e^- > h^+ > {}^{\bullet}O_2^-$, indicating that $^{\bullet}OH$ played a pivotal role in the reaction. The generation of $^{\bullet}OH$ was monitored by EPR spectroscopy, which verified a continuous increase in signal intensity as the reaction time extended from 5 to 20 minutes (Fig. 6d). Furthermore, $^{\bullet}OH$ production showed a correlation with sulfur vacancy concentration. As shown in Fig. 6e, the highest fluorescence intensity corresponding to $^{\bullet}OH$ was observed for MS-3, followed by MS-2, while MS-1 exhibited the lowest yield, which is consistent with the trend observed in Fig. 6b. The contributions of the four reactive species were quantitatively evaluated by scavenging experiments over catalysts with varying sulfur vacancy concentrations. As shown in Fig. S8(a)–(d), the contribution of $^{\bullet}OH$ exhibited a clear dependency on the sulfur vacancy concentration, following the order: MS-3 (85.6%) > MS-2 (62.7%) > MS-4 (40.7%) > MS-1 (33.5%). This trend correlates with the catalytic performance, MS-3, with

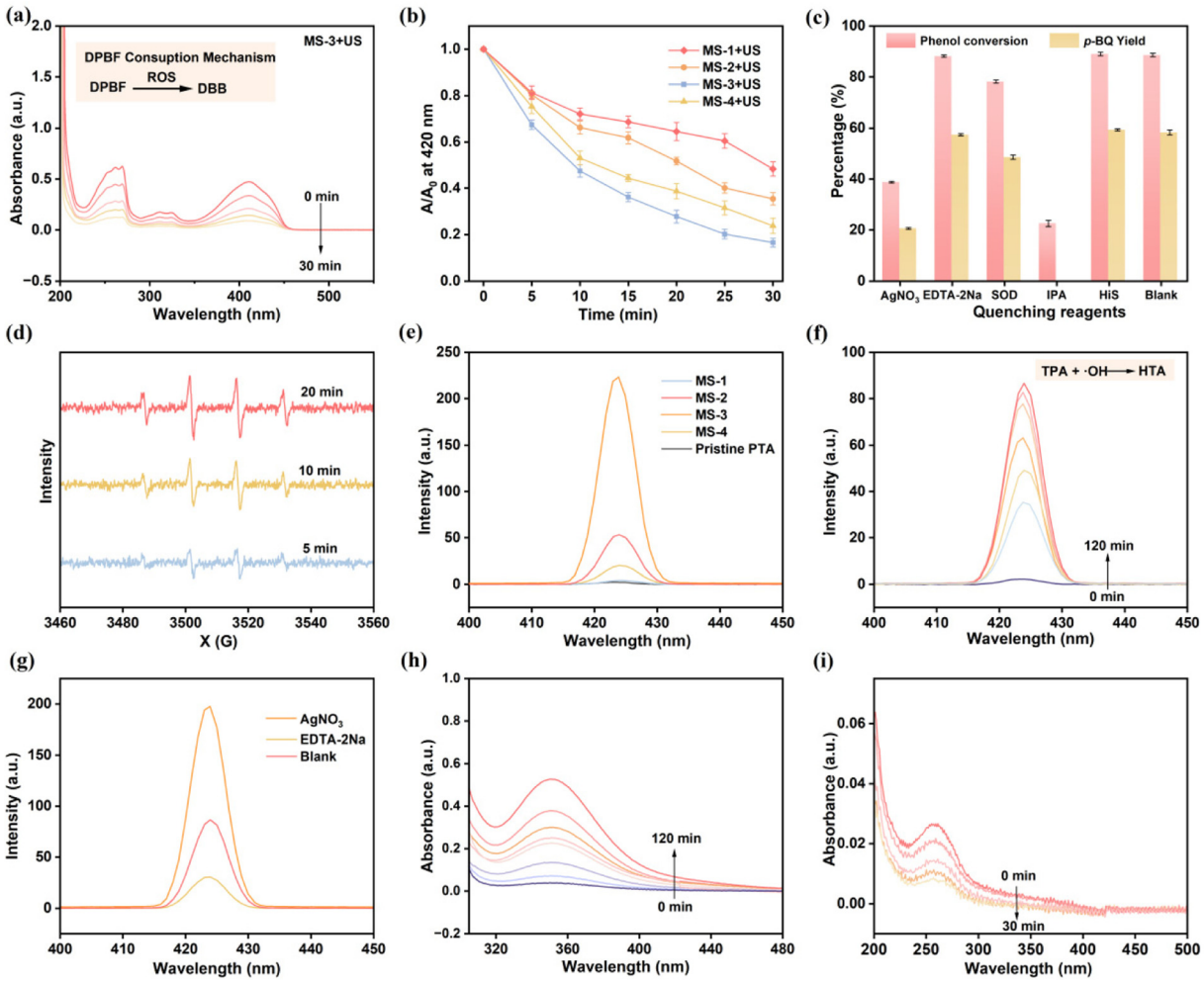

Fig. 6 (a) Time-dependent degradation of DPBF under MS-3 + ultrasound (US) treatment; (b) the absorbance decay ratio of DPBF under ultrasonic systems with different catalysts; (c) radical quenching experiments for identifying active species in MS-3; (d) spin-trapping DMPO-$^{\bullet}OH$ EPR; (e) fluorescence spectra of $^{\bullet}OH$ trapping in the presence of different quenchers; (f) time-dependent fluorescence intensity of $^{\bullet}OH$ in MS-3; (g) fluorescence spectra of $^{\bullet}OH$ trapping in the presence of different quenchers; (h) time-dependent concentration of H_2O_2; (i) time-dependent detection of $^{\bullet}O_2^-$.

moderate vacancy concentration, exhibited the highest phenol conversion and *p*-BQ yield. The results indicate that modulating the concentration of sulfur vacancies can selectively regulate the proportion of ˙OH in the reactive species, thereby driving the selective oxidation of phenol to *p*-BQ.

The generation of ˙OH is generally considered to proceed through two primary pathways[47,48] (i) it can be produced *via* the reaction between holes (h^+) and OH^- ions from water, or (ii) it can be formed through the reduction of oxygen by electrons (e^-) to H_2O_2, which is subsequently converted into ˙OH. Based on the previously discussed analysis of the MoS_2 band structure, the direct oxidation of water by holes is considered unlikely in this system, as the oxidation potential of H_2O/˙OH (1.99 V *vs.* NHE)[49] significantly exceeds the oxidative capability of the MoS_2 valence band. To clarify the actual origin of ˙OH, terephthalic acid (PTA) was first employed as a fluorescent probe, based on its reaction with ˙OH to form the highly fluorescent product 2-hydroxyterephthalic acid (HTA).[47] As shown in Fig. 6f, the fluorescence intensity was observed to increase gradually with reaction time, confirming the presence of ˙OH in MS-3. Furthermore, $AgNO_3$ and EDTA-2Na were separately introduced during the ultrasonic reaction, and the ˙OH-related fluorescence intensity was compared among the three systems after the same duration. As illustrated in Fig. 6g, the formation of ˙OH was significantly suppressed upon addition of $AgNO_3$ (an e^- scavenger), whereas the fluorescence intensity was notably enhanced when EDTA-2Na (an h^+ scavenger) was added. This observation can be attributed to the effective capture of holes by EDTA-2Na, which promotes the separation of electron–hole pairs, thereby allowing more electrons to participate in subsequent reactions and facilitating ˙OH generation. These results further supported the conclusion that the ˙OH formation pathway was predominantly governed by the electron-mediated process. To confirm the formation of H_2O_2 *via* the electron-mediated pathway, its concentration during the reaction was quantified by an iodometric method. As presented in Fig. 6h, H_2O_2 was detected, and its concentration was found to increase with prolonged reaction time. Finally, using nitroblue tetrazolium (NBT) as a specific probe for superoxide radicals (˙O_2^-), we successfully detected the ˙O_2^-

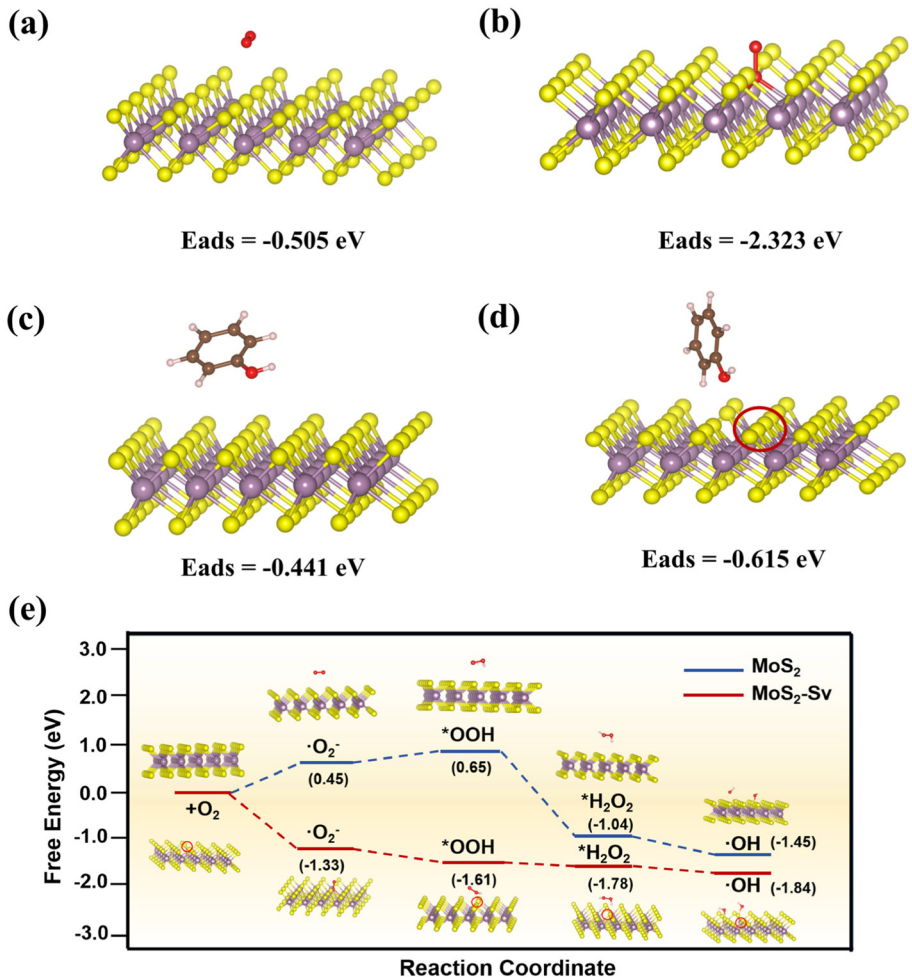

Fig. 7 Density functional theory calculations (DFT) of adsorption energies: oxygen on MoS_2 without (a) and with (b) a sulfur vacancy; phenol on MoS_2 without (c) and with (d) a sulfur vacancy; (e) free energy diagram obtained from DFT calculations.

signal in the reaction system (Fig. 6i), confirming that oxygen is effectively activated and transformed into a key reactive intermediate. To investigate whether the accumulated product *p*-BQ affects the generation of $^{\bullet}O_2^-$ during the reaction, we introduced *p*-BQ accumulated after 6 hours of reaction (approximately 0.14 mM) into the system and simultaneously monitored changes in $^{\bullet}O_2^-$ intensity using electron paramagnetic resonance (EPR) and probe experiments. As shown in Fig. S9a, the accumulation of *p*-BQ did not lead to significant quenching of the $^{\bullet}O_2^-$ signal, and no noticeable change in $^{\bullet}O_2^-$ signal intensity was observed *via* EPR (Fig. S9b). Based on quantitative EPR data, the concentration of $^{\bullet}O_2^-$ was measured to be 1.982×10^{-5} mol L^{-1} in the absence of *p*-BQ, while it remained at 1.886×10^{-5} mol L^{-1} in the presence of *p*-BQ, showing no significant reduction. This observation can be attributed to the fact that effective inhibition of radical reactions typically requires extremely high concentrations of quenchers, especially when the quenching process itself involves kinetic barriers. In this study, the *in situ* generated *p*-BQ concentration is insufficient to overcome the high activation energy barrier (0.91 eV) required for its reaction with $^{\bullet}O_2^-$, and kinetically, it cannot effectively compete with the rapidly generated $^{\bullet}O_2^-$ on the catalyst surface.[50] Therefore, it does not impede the continuous conversion of $^{\bullet}O_2^-$ to $^{\bullet}OH$. Furthermore, To directly elucidate the critical role of $^{\bullet}O_2^-$ in the generation pathway of $^{\bullet}OH$, we conducted validation through controlled experiments. A sufficient amount of superoxide dismutase (SOD) was added to the standard reaction system to quench $^{\bullet}O_2^-$, while the formation of $^{\bullet}OH$ was simultaneously monitored using the terephthalic acid fluorescence probe method and electron paramagnetic resonance (EPR) spectroscopy. As shown in Fig. S10a, the fluorescence intensity of $^{\bullet}OH$ decreased significantly upon quenching $^{\bullet}O_2^-$. Quantitative EPR analysis further revealed (Fig. S10b) that the concentration of $^{\bullet}OH$ was 1.264×10^{-5} mol L^{-1} in the absence of SOD, which dropped to 2.667×10^{-6} mol L^{-1} upon addition of SOD. Based on these results, the contribution of $^{\bullet}O_2^-$ to $^{\bullet}OH$ generation was estimated to be approximately 78.9%. These findings consistently demonstrate that $^{\bullet}O_2^-$ serves as an essential and critical precursor for $^{\bullet}OH$ generation in this system.

Based on the above analysis, the generation pathway of $^{\bullet}OH$ is likely to proceed *via* the following sequence: $O_2 \rightarrow {}^{\bullet}O_2^- \rightarrow H_2O_2 \rightarrow {}^{\bullet}OH$.

The introduced sulfur vacancies create coordinatively unsaturated Mo atoms in MoS_2, which modulate the electronic structure and generate unpaired electrons, resulting in highly active sites for reactant adsorption.[51] As shown in Fig. S11, the influence of the reaction atmosphere on the catalytic performance was investigated by comparing the results in air and nitrogen. In an air atmosphere, the phenol conversion reached approximately 88.59% with a *p*-BQ yield of 58.26%. In contrast, under a nitrogen atmosphere, the phenol conversion dropped significantly to 9.1%, and the formation of *p*-BQ was almost completely suppressed. These results indicate that oxygen plays a critical role in the catalytic reaction.

To further elucidate the activation mechanism of oxygen, density functional theory (DFT) calculations were performed to

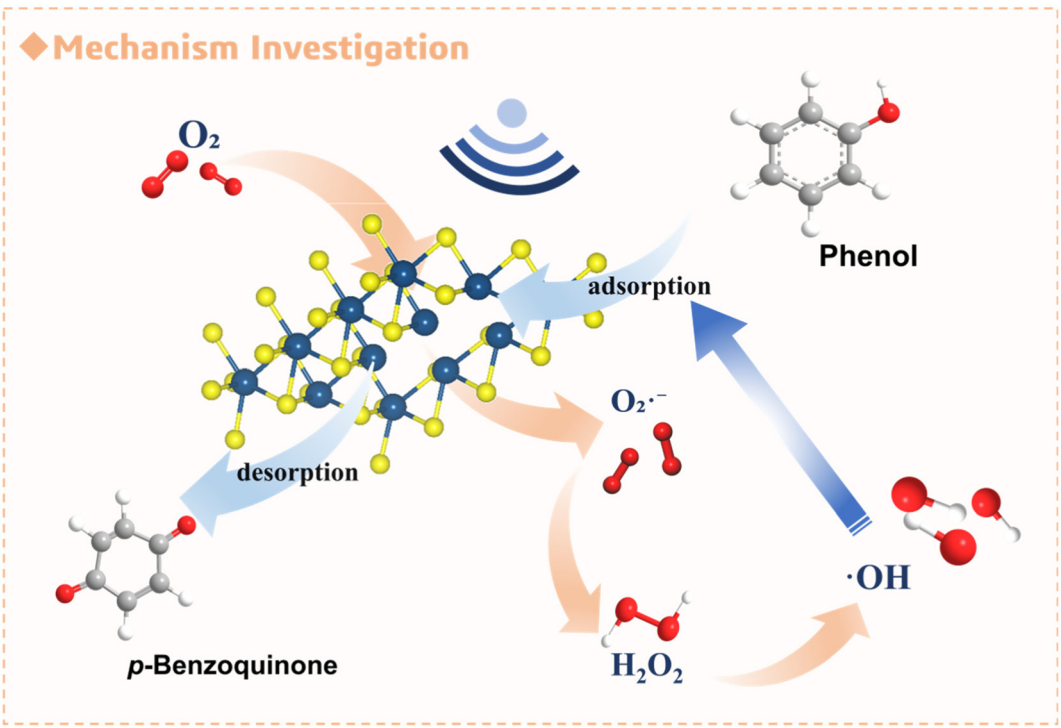

Fig. 8 Mechanism of piezocatalytic conversion of phenol to *p*-BQ.

compare the adsorption energies of oxygen on MoS_2 with sulfur vacancies and on pristine MoS_2. The top views of both the defective and pristine models provided in Fig. S12 for comparison. As presented in Fig. 7a and b, the adsorption energies of oxygen on pristine MoS_2 and MoS_2 with sulfur vacancy were calculated to be −0.505 eV and −2.323 eV, respectively. The difficulty of adsorption is determined by the magnitude of the adsorption energy.[52] The presence of sulfur vacancies significantly enhances the adsorption of oxygen on the material surface. Oxygen molecules adsorbed at the vacancy sites are more readily activated and transformed into highly reactive species, thereby driving subsequent reactions. The adsorption energy of phenol was −0.441 eV on pristine MoS_2 and −0.615 eV on the sulfur-deficient surface (Fig. 7c and d). This significant enhancement confirms that sulfur vacancies facilitate phenol adsorption. It is worth noting that the adsorption energy of *p*-BQ on sulfur-deficient MoS_2 was −0.553 eV (Fig. S13) and its absolute value is lower than that of phenol on the same site. This suggests that *p*-BQ can desorb more easily from the active sites. This timely desorption behavior effectively prevents further oxidation of the product, thereby ensuring the high selectivity toward *p*-BQ.

To elucidate the underlying catalytic mechanism, we conducted density functional theory (DFT) calculations to simulate the Gibbs free energy profile for the conversion of O_2 to $^{\bullet}OH$ (Fig. 7g). The results indicate that on pristine MoS_2, the activation of O_2 to form $^{\bullet}O_2^-$ is the rate-determining step, presenting a reaction barrier of 0.45 eV that severely impedes the process. In contrast, the introduction of sulfur vacancies fundamentally alters this pathway: not only does it render the initial activation of O_2 highly spontaneous and exothermic (ΔG = −1.33 eV), but it also ensures that all subsequent conversion steps remain thermodynamically favorable. This finding theoretically confirms that sulfur vacancies serve as the key active sites for promoting $^{\bullet}OH$ generation, with their central role lying in eliminating the kinetic barrier of the reaction and thereby significantly enhancing the overall catalytic performance.

4. Conclusion

This study employed a one-step hydrothermal method by adjusting the thiourea precursor concentrations to successfully synthesize MoS_2 catalysts with different sulfur vacancy concentrations. Their performance in the piezoelectric catalytic conversion of phenol to *p*-BQ was systematically investigated. The results demonstrated that the catalyst with a moderate concentration of sulfur vacancies exhibited optimal catalytic performance, achieving 92.57% phenol conversion, 66.56% *p*-BQ yield, and 71.9% selectivity after 6 hours of reaction.

The successful synthesis of MoS_2 with different sulfur vacancy concentrations was confirmed by EPR spectroscopy. Structural characterizations including SEM, XRD, XPS, and Raman spectroscopy revealed that the introduction of sulfur vacancies reduced the crystallinity and symmetry of the material. PFM measurements confirmed that sulfur vacancies enhanced the piezoelectric coefficient of MoS_2 by 1.3 to 7.4 times. At a moderate vacancy concentration, the maximum piezoelectric displacement increased from 800 pm to 11 nm. Further analyses by PL, EIS, and piezoelectric current response tests indicated that sulfur vacancies effectively promoted the separation and transfer of polarized charges: the charge separation efficiency increased by approximately 4-fold, while the piezoelectric current response was enhanced by about 2.7-fold compared to pristine MoS_2. Mott–Schottky tests under ultrasonic irradiation demonstrated band bending in the material, which contributed to improved charge carrier separation efficiency and thus optimized the piezoelectric catalytic process.

Quenching experiments and electron paramagnetic resonance (EPR) spectroscopy collectively confirmed that the reaction follows a pathway dominated by $^{\bullet}OH$ radicals. By analyzing the contribution of various reactive species in different catalyst systems, we found that sulfur vacancy engineering can selectively regulate the proportion of $^{\bullet}OH$ among the reactive species. The MoS_2 with moderate sulfur vacancies exhibited the highest $^{\bullet}OH$ contribution, thus demonstrating the optimal catalytic selectivity and conversion efficiency. Probe experiments further indicated that the formation pathway of $^{\bullet}OH$ is likely as follows: $O_2 \rightarrow {}^{\bullet}O_2^- \rightarrow H_2O_2 \rightarrow {}^{\bullet}OH$. Atmosphere control experiments combined with theoretical calculations demonstrated that sulfur vacancies played a key role in the oxygen activation process. DFT calculations further confirmed that sulfur vacancies actively facilitated the adsorption of phenol and the desorption of *p*-BQ.

The core innovation of this work lies in revealing the dual functionality of sulfur vacancies, serving as active sites for phenol adsorption and selectively regulating the proportion of $^{\bullet}OH$ among the reactive species. The generated $^{\bullet}OH$ can further oxidize the adsorbed phenol to *p*-BQ. Meanwhile, the adsorption energy of *p*-BQ on sulfur vacancies is lower than that of phenol, which promotes its preferential desorption and thereby ensures the efficient operation of the catalytic process. A schematic diagram of the proposed reaction mechanism is presented in Fig. 8.

In summary, this work demonstrates that the selective regulation of the $^{\bullet}OH$ proportion among reactive species *via* sulfur vacancy engineering enables high selective piezoelectric conversion performance, providing a new strategy for utilizing lignin derivatives to synthesize aromatic chemicals.

Author contributions

Xinlei Ma: writing – original draft, methodology, investigation, validation, formal analysis, data curation, conceptualization. Bo Zhang: writing – review & editing, supervision, resources, investigation, funding acquisition, conceptualization. Xin Huang: writing – original draft, methodology, investigation, validation, formal analysis, data curation. Qing Xu: writing – review & editing, supervision. Roger Ruan: writing – review & editing, supervision.

Conflicts of interest

The authors declare that they have no known competing financial interests or personal relationships that could have appeared to influence the work reported in this paper.

Data availability

The data supporting this article have been included as part of the supplementary information (SI). Supplementary information is available. See DOI: https://doi.org/10.1039/d5gc06083d.

Acknowledgements

This work is supported by the Natural Science Fund Program of China (No. 52376171 & 52476190), and the Science and Technology Project of Jiangsu Province (No. BE2022604 & BE2021701).

References

1 H. Li, P. Duan, Y. Huang, C. Cui, F. Hollmann, Y. Ma, Y. Wang, J. Zhang, W. Liu and W. Zhang, *ACS Catal.*, 2024, **14**, 1733–1740.
2 Z. Shen, G. Zhang, C. Shi, J. Qu, L. Pan, Z. Huang, X. Zhang and J.-J. Zou, *Fuel*, 2023, **334**, 126634.
3 Y. Chen, W. Ying and M. Harmata, *Tetrahedron Lett.*, 2011, **52**, 480–482.
4 R. Wu, Q. Meng, J. Yan, H. Liu, Q. Zhu, L. Zheng, J. Zhang and B. Han, *J. Am. Chem. Soc.*, 2022, **144**, 1556–1571.
5 P. Silakari, Priyanka and P. Piplani, *Mini-Rev. Med. Chem.*, 2020, **20**, 1586–1609.
6 M. Yang, Y. Tan, G. Yang, X. Chang, T. Tian, W.-G. Li, Y. Fang, J. Shen, S. Yang and W.-Q. Wu, *Angew. Chem., Int. Ed.*, 2025, **64**, e202415966.
7 J. Wu and M. C. Kozlowski, *Org. Lett.*, 2023, **25**, 907–911.
8 H. Zheng, Y. Wang, J. Liu, J. Wang, K. Yan and K. Zhu, *Appl. Catal., B*, 2024, **341**, 123335.
9 P. Jia, J. Li and H. Huang, *Adv. Funct. Mater.*, 2024, **34**, 2407309.
10 K. Kubota, Y. Pang, A. Miura and H. Ito, *Science*, 2019, **366**, 1500–1504.
11 H. Liu, S. Li, M. Liu, P. Sun, X. Zhang, L. Zhang, Y. Zhang, G. Contreras-Jiménez, J. Potier, Z. Sun, X. Yan, Y. Wan, L.-D. Zhao and J. Zhang, *Nano Energy*, 2025, **142**, 111241.
12 A. K. Verma, M. A. Rahman, P. Vashishtha, X. Guo, M. Sehrawat, R. Mitra, S. P. Giridhar, M. Waqar, A. Bhoriya, B. J. Murdoch, C. Xu, A. Zavabeti, W. Q. Song, Y. Li, S. R. Dhakate, B. Gahtori, T. Ahmed, I. H. Abidi and S. Walia, *ACS Nano*, 2025, **19**, 3478–3489.
13 J. Zhu, Q. Ji, P. Lu, W. Zhou, Q. Zhong, K. Zhang, Y. Liu, G. Zuo, Z. Xu, S. Yang, L. Zhang and H. He, *Adv. Funct. Mater.*, 2025, **35**, 2419597.
14 C. Lin, G. Fan, J. Luo, C. Cai, X. Cao and K.-Q. Xu, *Chem. Eng. J.*, 2025, **520**, 166094.
15 M. Yang, B. Ding, X. Ma, J. Li, D. Han, S. Liu, Z. Liu, J. Tan, H. Chen, P. Zheng, P. A. Ma and J. Lin, *Angew. Chem., Int. Ed.*, 2025, **64**, e202507502.
16 Y.-M. Chen, Y.-C. Chen, K.-Y. Tu, Y.-D. Lin, Y.-G. Lin, H.-Y. Lin, S. Bajaj and J. M. Wu, *Small*, 2025, e08162.
17 Y. Luo, G. Chen, Z. Wang, S. Zhang, X. Zheng, S. Meng and S. Chen, *Adv. Sci.*, 2025, **12**, e04167.
18 Y. Xi, C. Zhang, W. Tu, Y. Guo, T. Bao, Y. Zou, C. Liu and C. Yu, *Angew. Chem., Int. Ed.*, 2025, **64**, e202505046.
19 S. Niu, J. Cai and G. Wang, *Nano Res.*, 2021, **14**, 1985–2002.
20 J. Chen, C. Zhang, M. Huang, J. Zhang, J. Zhang, H. Liu, G. Wang and R. Wang, *Appl. Catal., B*, 2021, **285**, 119810.
21 M. Fan, K. Zhang, X. Gu, Y. Mei, R. Chen, J. Hu, H. Hou and J. Yang, *Chem. Eng. J.*, 2025, **521**, 166654.
22 L. Guan, Q. Zhang, M. Cen, B. Chen, W. Peng, Y. Li, D. Xu and X. Fan, *ACS Catal.*, 2025, **15**, 6535–6543.
23 S. Mondal, K. Rajan, L. Patra, M. Rathinam and V. Ganesh, *Small*, 2025, **21**, 2411828.
24 L. Li, Q. Han, L. Wang, B. Liu, K. Wang and Z. Wang, *Chem. Eng. J.*, 2022, **440**, 135866.
25 C. Zhong, J. Wang, Y. Liu, C. Zhang, Z. Li, Z. Liu, C. Zhao, L. Yang and X. Xu, *Appl. Catal., B*, 2025, **370**, 125193.
26 X. Jiang, R. Wang, Y. Tang, W. Di, W. Wang, B. Zhao and L. Yang, *Adv. Funct. Mater.*, 2025, **35**, 2418412.
27 H. Peng, H. Yang, J. Han, X. Liu, D. Su, T. Yang, S. Liu, C.-W. Pao, Z. Hu, Q. Zhang, Y. Xu, H. Geng and X. Huang, *J. Am. Chem. Soc.*, 2023, **145**, 27757–27766.
28 H. Feng, Y. Li, Y. Gu, X. Liu, L. Zhang, Z. Wang and Z. Li, *Appl. Catal., B*, 2025, **365**, 124862.
29 X. Ma, B. Ding, Z. Yang, S. Liu, Z. Liu, Q. Meng, H. Chen, J. Li, Z. Li, P. A. Ma and J. Lin, *J. Am. Chem. Soc.*, 2024, **146**, 21496–21508.
30 F.-R. Hsu, Y.-C. Chen, C.-H. Yeh, H.-Y. Lin, H.-Y. T. Chen and J. M. Wu, *Nano Energy*, 2025, **142**, 111270.
31 K. Wang, C. Han, J. Li, J. Qiu, J. Sunarso and S. Liu, *Angew. Chem., Int. Ed.*, 2022, **61**, e202110429.
32 W. Liu, C. Zhang, J. Shi, Z. Yu, Z. Fu, C. Cheng, X. Guan, M. Liu and L. Guo, *Appl. Catal., B*, 2026, **381**, 125858.
33 W. Song, C. Wang, Y. Liu, K. C. Chong, X. Zhang, T. Wang, Y. Zhang, B. Li, J. Tian, X. Zhang, X. Wang, B. Yao, X. Wang, Y. Xiao, Y. Yao, X. Mao, Q. He, Z. Lin, Z. Zou and B. Liu, *J. Am. Chem. Soc.*, 2024, **146**, 29028–29039.
34 D. Dai, J. Qiu, J. Xu, G. Xia, Y. Li, B. Fang and J. Yao, *ACS Catal.*, 2025, **15**, 16513–16521.
35 Y. Wu, P. T. T. Nguyen, S. S. Wong, M. Feng, P. Han, B. Yao, Q. He, T. C. Sum, T. Zhang and N. Yan, *Nat. Commun.*, 2025, **16**, 846.
36 A. Syari'ati, S. Kumar, A. Zahid, A. El Yumin, J. Ye and P. Rudolf, *Chem. Commun.*, 2019, **55**, 10384–10387.
37 Y. Zhang, H. Li, X. Zhang, H. Zhang, W. Zhang, H. Huang, H. Ou and Y. Zhang, *J. Colloid Interface Sci.*, 2023, **630**, 742–753.

38 R. Li, D. Zhang, J. Wei, B. Li, H. Xin, H. Pengjie, Z. Ni, D. Yang and X. Yu, *Joule*, 2025, **9**, 102141.
39 Z. Sha, C. Hu, S. Tu, T. Li, F. Chen and H. Huang, *Nano Energy*, 2025, **139**, 110919.
40 X.-Q. Qiao, H. Guo, P. Du, B. Sun, D. Hou, M. Wang, X. Wu, S. Huang, C. Sun, T. Wu and D.-S. Li, *J. Energy Chem.*, 2026, **113**, 1–11.
41 M. Xu, X. Ruan, D. Meng, G. Fang, D. Jiao, S. Zhao, Z. Liu, Z. Jiang, K. Ba, T. Xie, W. Zhang, J. Leng, S. Jin, S. K. Ravi and X. Cui, *Adv. Funct. Mater.*, 2024, **34**, 2402330.
42 J. Qin, C. Xi, R. Zhang, T. Liu, P. Zou, D. Wu, Q. Guo, J. Mao, H. Xin and J. Yang, *ACS Catal.*, 2021, **11**, 4486–4497.
43 J. Mao, J. He, W. F. Io, F. Guo, Z. Wu, M. Yang and J. Hao, *ACS Nano*, 2024, **18**, 30360–30367.
44 H. Peng, W. Miao, J. Zeng, Z. Wang, C. Yan, G. Ma and Z. Lei, *Adv. Sci.*, 2025, **12**, 2417288.
45 Y. Zhang, J. Wang, L. Shan, B. Han, Q. Gao, Z. Cai, C. Zhou, X. Tian, R. Sun and L. Mai, *Adv. Energy Mater.*, 2024, **14**, 2303464.
46 F. Yang and Y. Zhao, *Nano Energy*, 2024, **131**, 110270.
47 T. Ren, W. Tian, Q. Shen, Z. Yuan, D. Chen, N. Li and J. Lu, *Nano Energy*, 2021, **90**, 106527.
48 J. Xu, K. Gu, P. Wang, P. Cheng, H. Che, C. Tang, K. Zhang and Y. Ao, *Nat. Commun.*, 2025, **16**, 7908.
49 X. Zhang, Y. Chen, R. Guo, Z. Zhang, Z. Sun, Y. Zhang and F. Yan, *Appl. Catal., B*, 2025, **372**, 125314.
50 J. Zhang, G. Zhang, H. Lan, M. Sun, H. Liu and J. Qu, *Environ. Sci. Technol.*, 2023, **57**, 12117–12126.
51 T. Zhou, J. Deng, Y. Chu, X. Peng, Y. Yang, Z. Wang, Y. Zeng, B. Song, M. Cheng and C. Zhou, *Appl. Catal., B*, 2026, **381**, 125892.
52 J. Pan, Y. Liu, Q. Lin, Y. Deng, Y. Luo, Z. Zhao, L. Wei, J. Huang and J. Wang, *J. Hazard. Mater.*, 2025, **486**, 137008.